Journal of Geophysical Research

Supporting Information for

Small-scale thermal upwellings under the Northern East African Rift from *S* travel-time tomography

Chiara Civiero[1], Saskia Goes[1], James O. S. Hammond[2], Stewart Fishwick[3], Abdulhakim Ahmed[4,5], Atalay Ayele[6], Cecile Doubre[7], Berhe Goitom[8], Derek Keir[9], J. Michael Kendall[8], Sylvie Leroy[4], Ghebrebrhan Ogubazghi[10], Georg Rumpker[11] and Graham W. Stuart[12]

(1) Dept. Earth Sci. & Eng., Imperial College London, UK; (2) Department of Earth and Planetary Science, Birkbeck, University of London, UK (3) Department of Geology, University of Leicester, UK; (4) Sorbonne Universités, UPMC Univ Paris 06, UMR 7193, Institut des Sciences de la Terre Paris, France; (5) Seismological and Volcanological Observatory Center, Dhamar, Yemen; (6) Institute of Geophysics, Space Science and Astronomy, Addis Ababa University, Ethiopia; (7) Institut de Physique du Globe, Université de Strasbourg/EOST, Strasbourg, France; (8) School of Earth Sciences, University of Bristol, UK; (9) National Oceanography Centre Southampton, University of Southampton, UK (10) Eritrea Institute of Technology, Asmara, Eritrea, (11) Department of Geophysics, Goethe University Frankfurt, Germany; (12) School of Earth and Environment, University of Leeds, UK

Contents of this file

Part 1: slices through Fishwick (2010) surface wave model – Figure S1
Part 2: additional S inversions and P model – Figures S2-S7
Part 3: additional resolution tests – Figures S8-S11
Part 4: additional figures for seismic ratios, thermal interpretation – Figures S12-S15
Part 5: station information – Table S1
References

Introduction

The supporting information contains additional figures to further illustrate the resulting models and their resolution. In addition, it contains, to facilitate comparison, figures from our previously published P model, NEAR-P15 [*Civiero et al.*, 2015]. The supplementary table contains the details of all the stations and networks from which data were used in this study.

Part 1 – Surface wave model used as reference in damped inversions

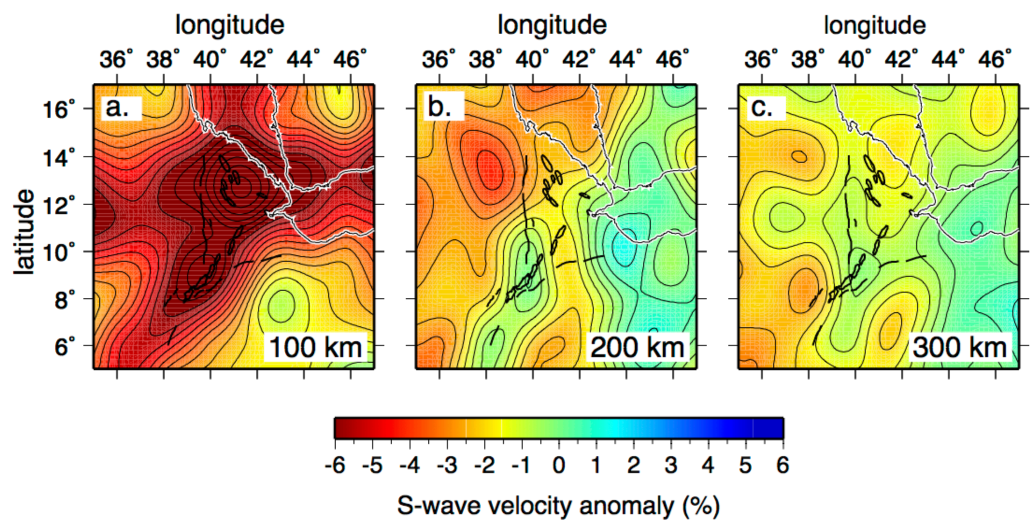

Figure S1. Depth slices showing the V_S anomalies from surface wave model from *Fishwick* (2010), which is used as 3-D reference model in the top 350 km for our damped inversions. The model covers all of Africa, but is only shown for our study region. The anomalies are relative to the average velocity-depth profile for the whole *Fishwick* (2010) model. The spacing between the contours is 0.50%. Note the anomaly scale is twice that of Fig S2 and others of our inverted model to allow displaying the structures at 100 km depth. Black lines delineate the major border faults and magmatic zones bounding the Afar Depression and black over white lines show coastlines.

Part 2 - Additional *S* inversions and *P* model

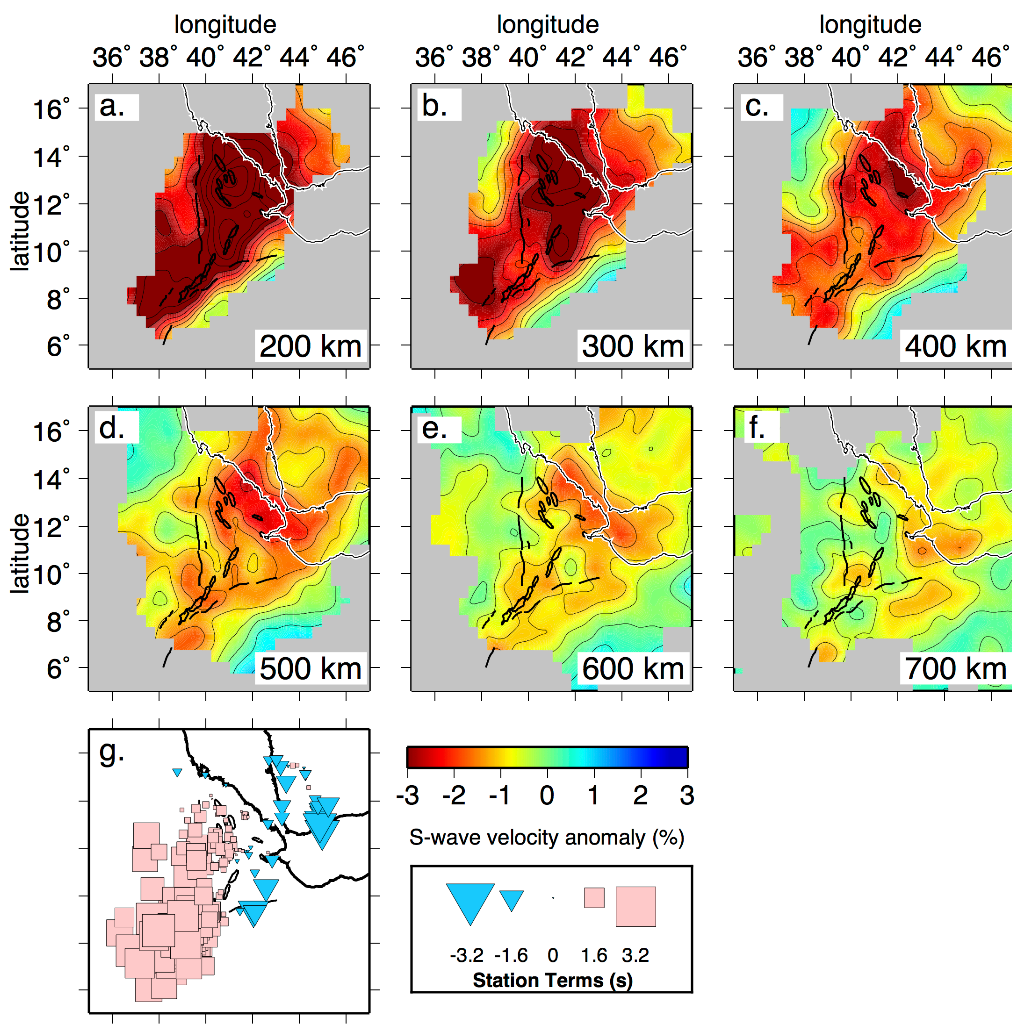

Figure S2. Depth slices through the *S-SKS*-time *preferred intermediate damped* tomographic model (flattening=4800, smoothing=153600, damping=35) at depths between 200 and 700 km. Regions with *less than 10 rays per node are shaded gray*. The spacing between the contours is 0.50%. Black lines delineate the major border faults and magmatic zones bounding the Afar Depression and black over white lines show coastlines. Triangular and square symbols in panel h represent the sign and magnitude of the station static terms. Comparison with Fig. 4 shows that the key features discussed in the text are all crossed by at least 10 rays per node.

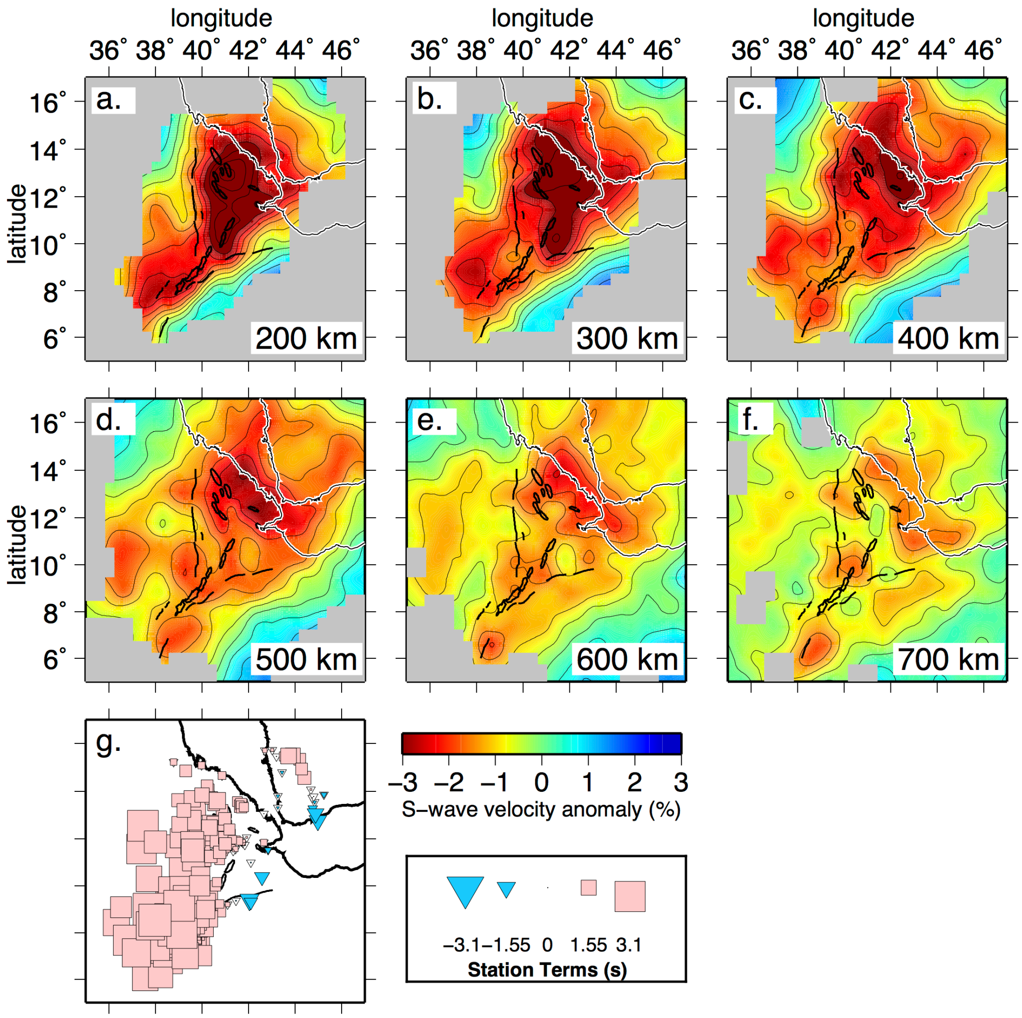

Figure S3. Depth slices through the *S-SKS*-time *undamped* tomographic model (flattening=4800, smoothing=153600, damping=0) at depths between 200 and 700 km. Regions with less than 5 rays per node are shaded gray. The spacing between the contours is 0.50%. Black lines delineate the major border faults and magmatic zones bounding the Afar Depression and black over white lines show coastlines. Triangular and square symbols in panel h represent the sign and magnitude of the station static terms. These depth slices illustrate that as in our preferred damping model in Fig. 4, the clusters of low-velocity anomalies that first appear around 200 km depth persist throughout the transition zone.

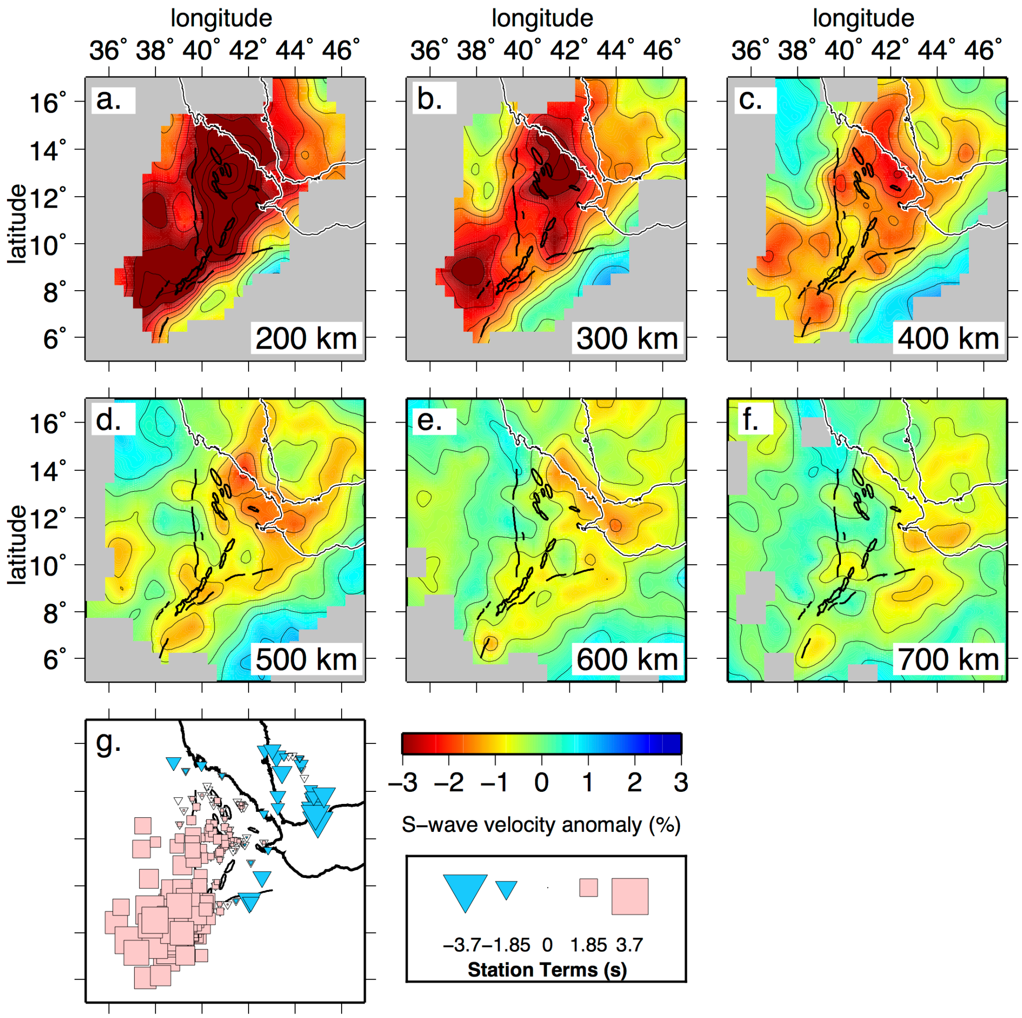

Figure S4. Depth slices through an *S-SKS* inversion with our preferred flattening (4800) and smoothing (153600) parameters but with a *stronger degree of damping* = 70. Triangular and square symbols in panel h represent the sign and magnitude of the station static terms. Regions with less than 5 rays per node are shaded grey. The spacing between the contours is 0.50%. Black lines delineate the major border faults and magmatic zones bounding the Afar Depression and black over white lines show coastlines. Structures are similar to those in our model with preferred damping (Fig. 4), but anomaly amplitudes decrease more strongly with depth.

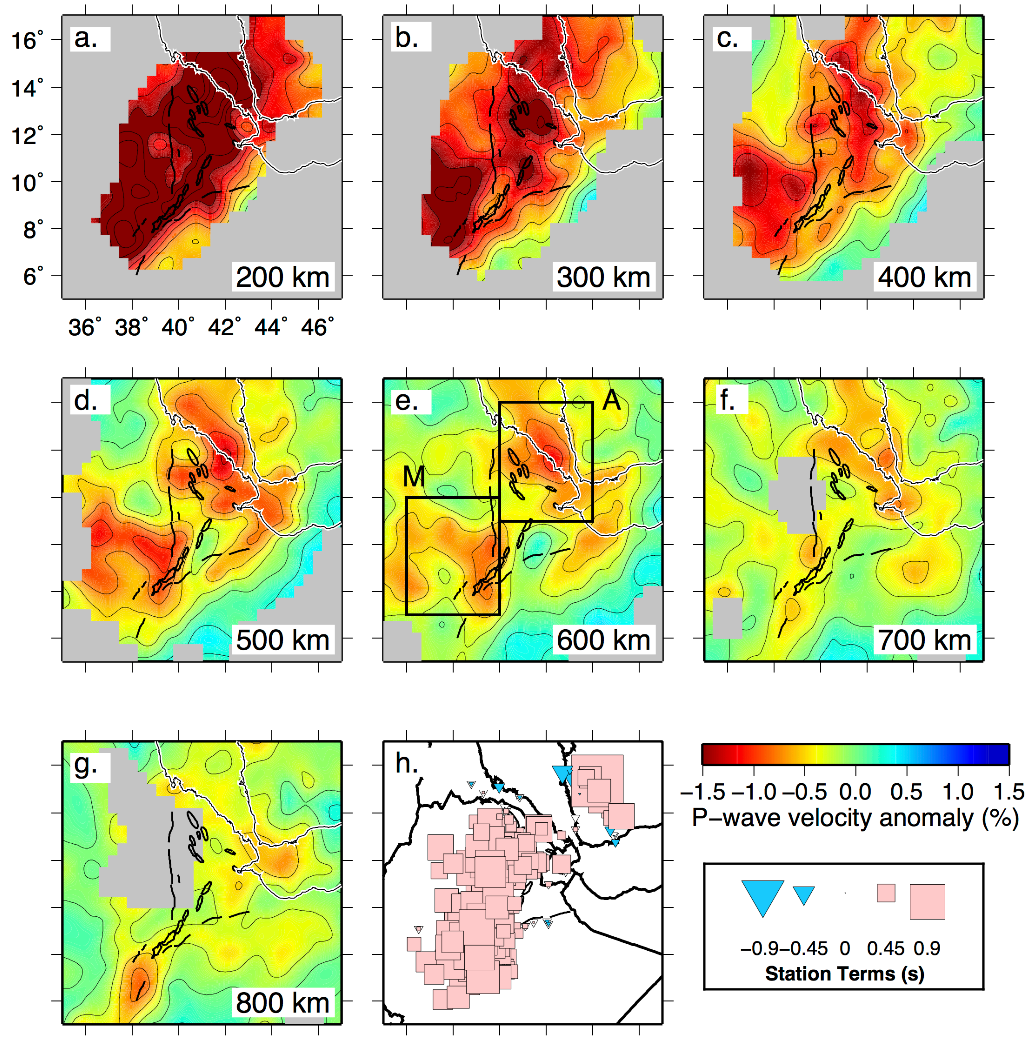

Figure S5. Depth slices through tomographic *P model* NEAR-P15 with preferred damping (flattening=4800, smoothing=153600, damping = 35) from *Civiero et al.* [2015], at depths between 200 and 800 km. Triangular and square symbols in panel h represent the sign and magnitude of the station static terms. Regions with less than 5 rays per node are shaded grey. The spacing between the contours is 0.25%. Black lines delineate the major border faults and magmatic zones bounding the Afar Depression and black over white lines show coastlines. The two boxes covering Afar (A) and an area west of the MER (M) in panel e. show the regions used in our temperature interpretation in Fig. 7. The structures in this model are very similar to those in NEAR-S16 (Fig. 4).

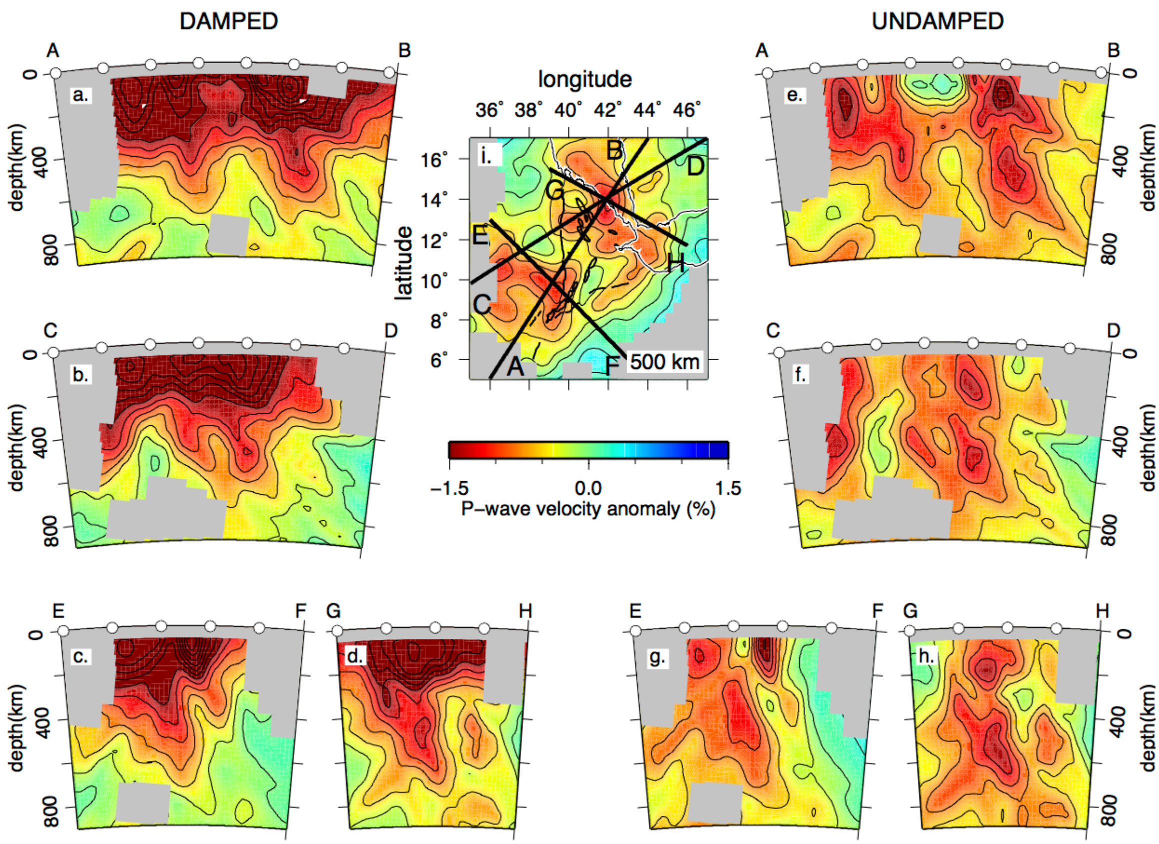

Figure S6. Vertical cross sections through the tomographic *P model* NEAR-P15 from *Civiero et al.* [2015] for preferred (damping=35) (a-d) and undamped (damping=0) cases (e-h) (both flattening=4800, smoothing=153600). The location of the cross-sections (black lines) is shown in the 500 km depth slice through the damped model (i). Regions with less than 5 rays per node are shaded grey. The spacing between the contours is 0.25%. White points indicate the distance every 2 degrees. Cross section A-B cuts through subvertical downwellings below Afar and west of the MER. C-D is a cross section through the prominent low-velocity anomalies in the Afar region and directly next to the MER. Section E-F cross cuts the anomaly next to the MER, while section G-H provides another view of the Afar low-velocity anomaly. The undamped models (e-h) illustrate the 100-200 km width of the low-velocity structures, while the damped models (a-d) emphasize the continuity between shallow and transition zone structure. Comparison with the S models (Fig. 5) reveals the similarity of the P and S structures.

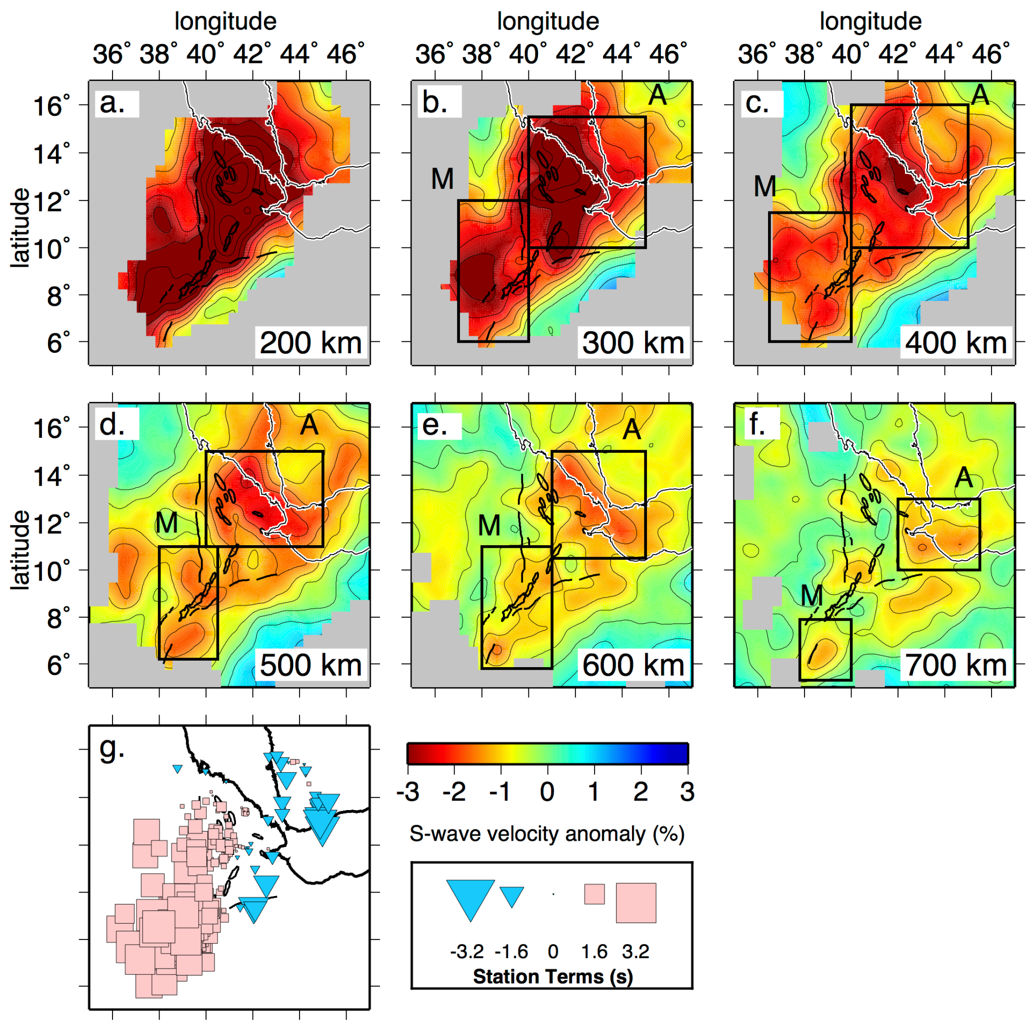

Figure S7. Depth slices through tomographic *S model NEAR-S16* with preferred damping (flattening=4800, smoothing=153600, damping = 35). Same as Fig. 4, but with superimposed a set of boxes covering Afar (A) and an area west of the MER (M) that delineate the regions used in our temperature interpretation in Fig. 7.

Part 3 – Additional resolution tests

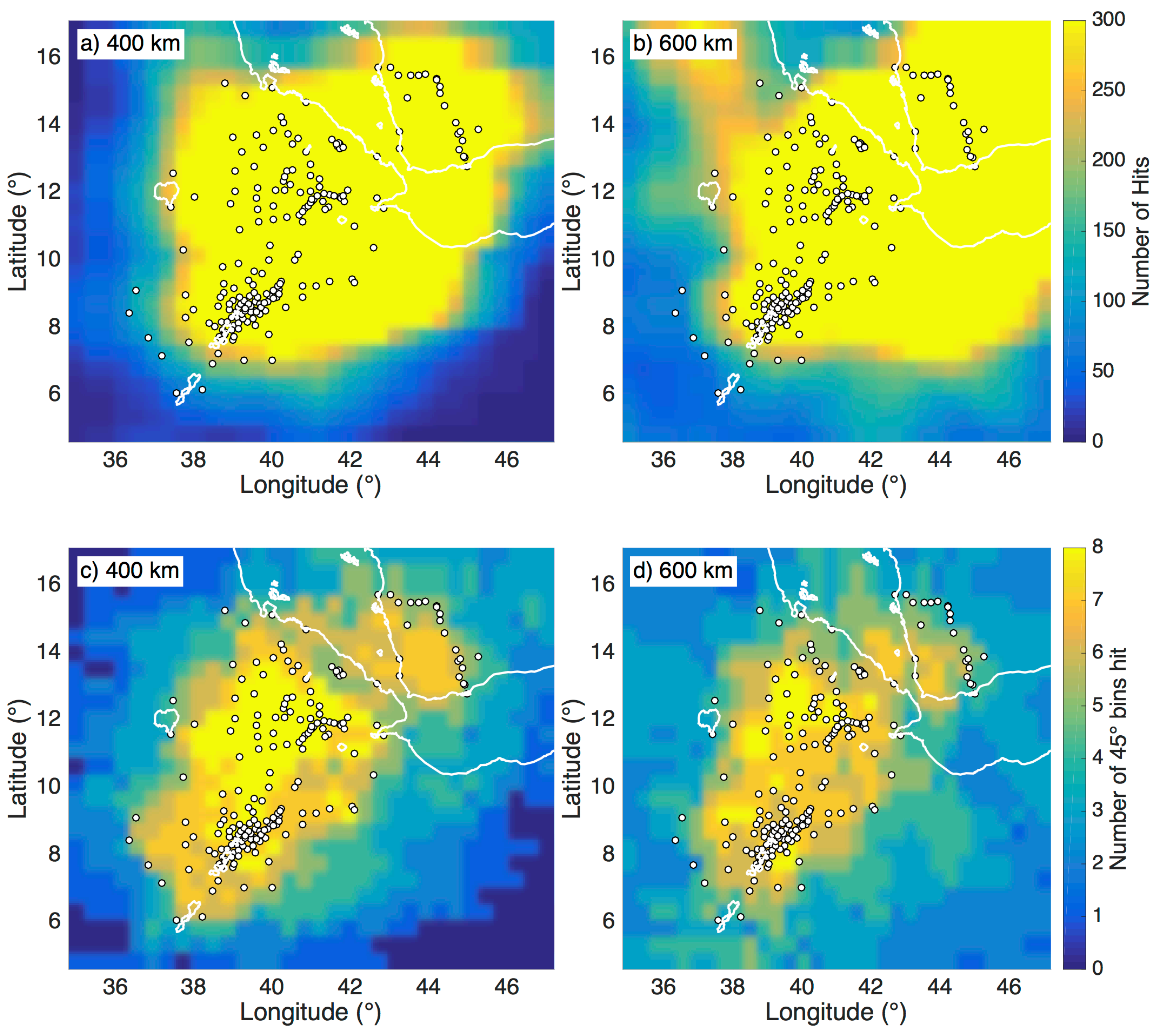

Figure S8. Maps comparing hit count (top) and crossing rays (bottom) at a depth of 400 km (a,c) , and 600 km (b,d) for the north-east East-African Rift. The azimuthal coverage is expressed as the number of different 45° bins that are crossed, where 8 would be a complete 360° coverage. a,b) Number of hits per node based on the rays used in this study at 400 and 600 km depth, respectively. c,d) Number of different 45° bins hit by rays at 400 and 600 km depth, respectively. Note the good coverage both in number of hits and crossing of rays. Coast lines and lakes are shown in white. White circles show seismic stations used in each study.

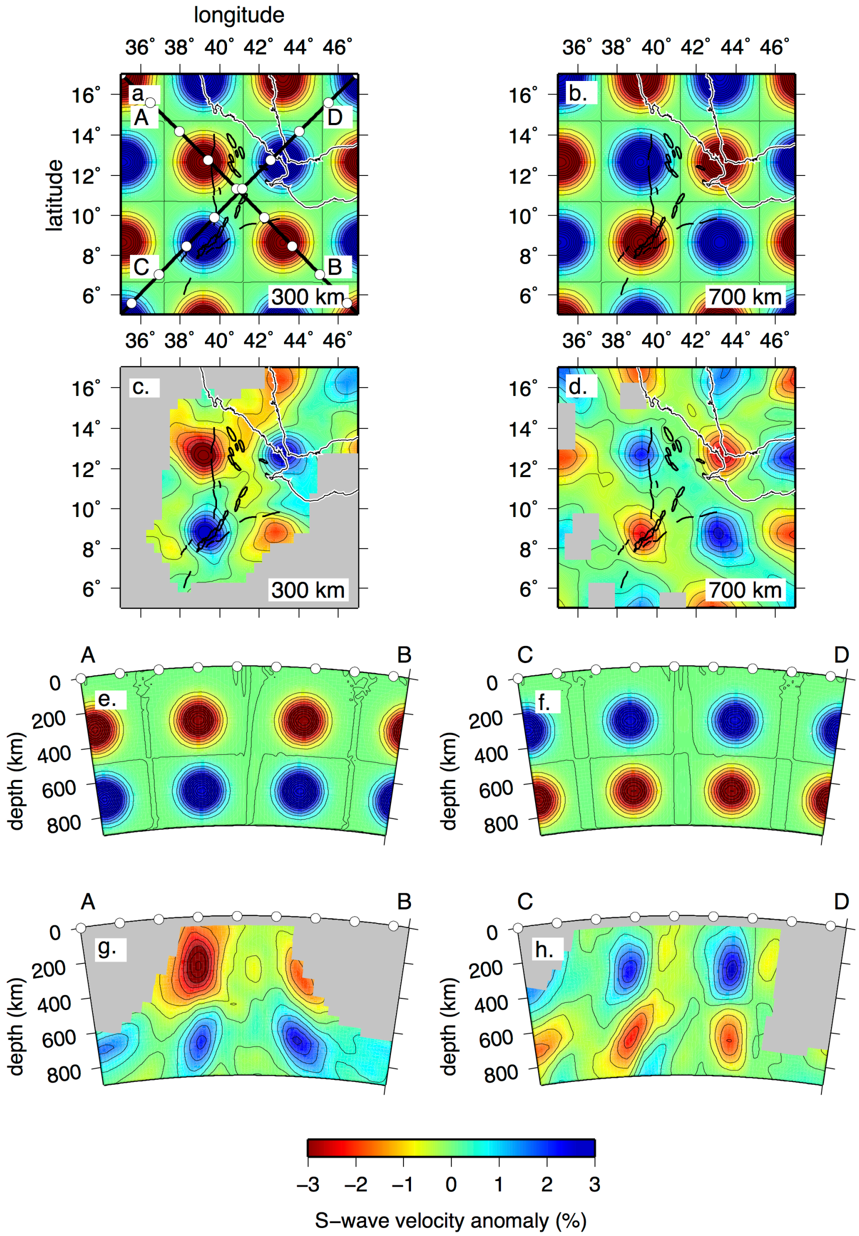

Figure S9. Checkerboard resolution tests for the *S-SKS*-times tomographic inversion, using 250 km wide spherical anomalies with a Gaussian amplitude profile, peaking at 7% (width defined as the distance to 20% of the maximum amplitude). The same raypaths and inversion parameters as in the data inversion are used and Gaussian noise of 0.37 s is added to mimic that in the data. Damping is not included, as this does not affect the spatial distribution of resolution. Regions with less than 5 rays per node are shaded grey. Contour interval is 0.50%. White circles along the top of the vertical profiles are spaced every 2°. (a, b) input model at 300 and 700 km depth. (c, d) Recovered checkers at 300 and 700 km depth. (e-h) vertical cross sections, oriented approximately rift-perpendicular (e,g) and approximately parallel to the rift trend (f,h), through the input (e,f), and output (g,h) models (orientations of the profiles are shown in depth slice a).

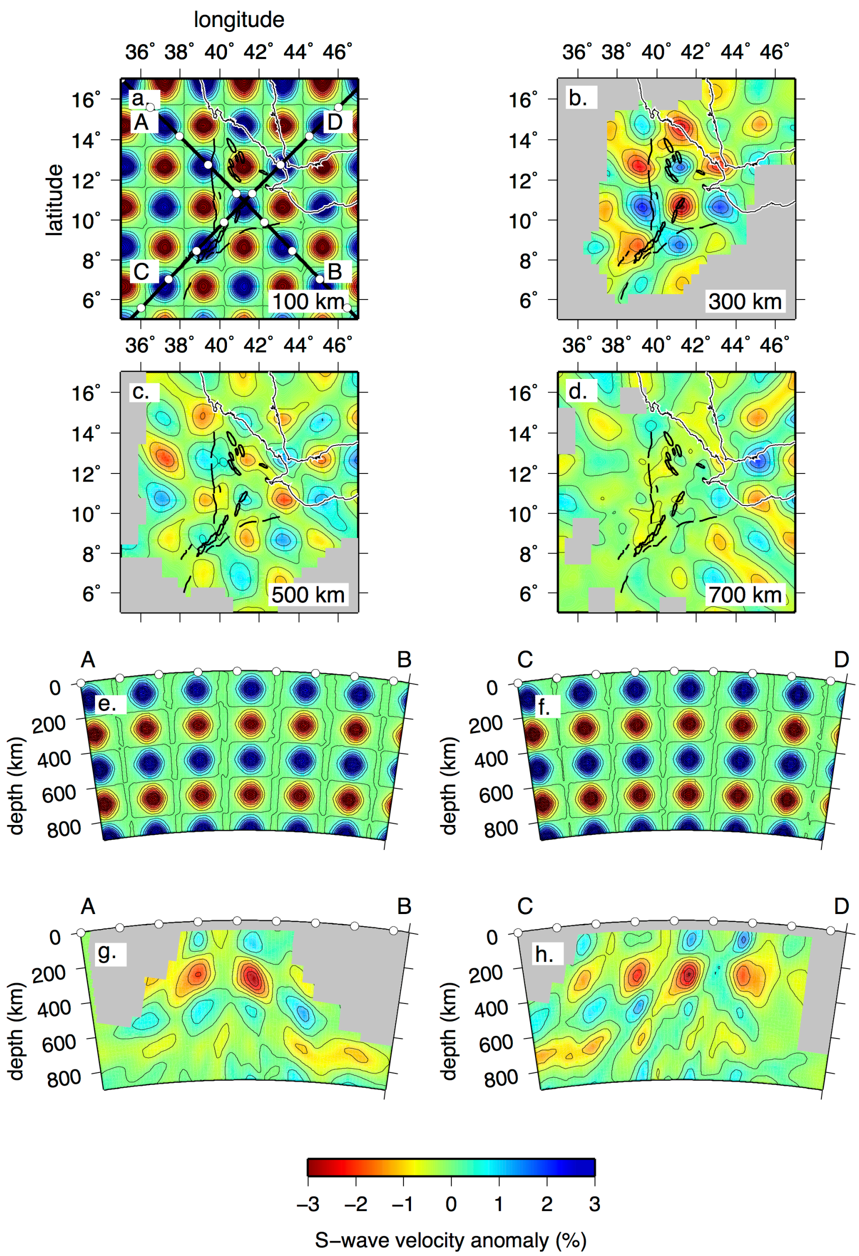

Figure S10. Checkerboard resolution test for the *S-SKS* inversion, as in Fig. S9, but with checkers of 125 km width, again with 7% peak amplitudes. (a) example of the input model at 300 km depth. (b,c,d) Recovered checkers at 300, 500 and 700 km depth, respectively. Panels (e-h) show vertical cross sections through the checker structure, oriented approximately rift-perpendicular (e,g) and rift-parallel (f,h), through the input (e,f), and output (g,h) models (orientations of the profiles are shown in depth slice a).

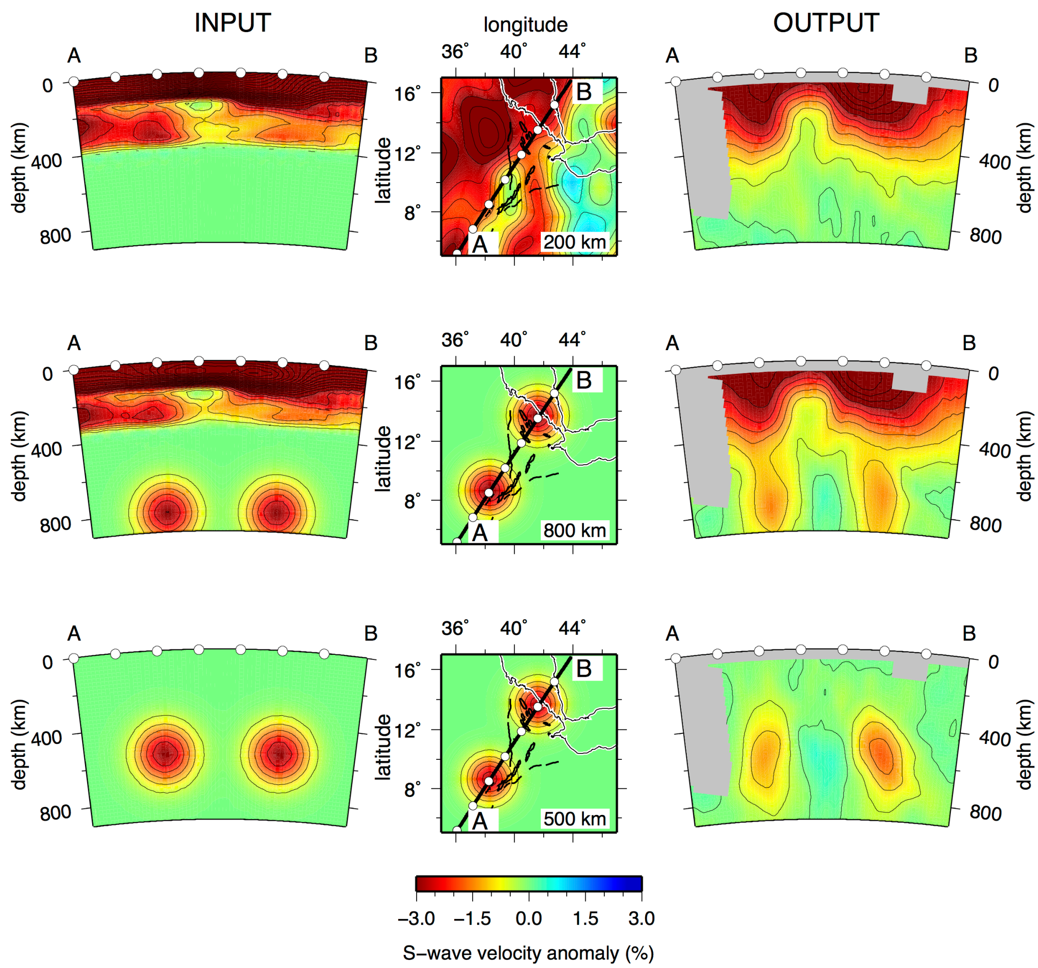

Figure S11. Three resolution tests along cross-section A-B for the *S-SKS* inversion; orientation is shown in the depth slices through each input model in the middle column (note the different depths of the slices for the different models). Regions with less than 5 rays per node are shaded gray. The spacing between the contours is 0.50%. White circles along the top of the vertical profiles mark the distance every 2°. The left-hand column shows synthetic input models and the right-hand column the corresponding recovered output models. The synthetic inversion is done using the same parameters as for the data-derived inversion. The synthetic test in the first row uses the *S*-structure estimated from the surface-wave model from Fishwick [2010] down to 350 km depth as the input model. The panels in the second row show a test with the same surface-wave-derived structure at shallow depths, plus a set of Gaussian low-velocity anomalies with peak amplitudes of 3.2% and a 380 km diameter (defined as the distance to 20% of the maximum amplitude) along line A-B, placed beneath the transition zone (centres at 800 km depth), to represent lower-mantle structure with a large excess temperature (~400°C). The third row shows a test using two low-velocity anomalies with 3.2% maximum-amplitude and 380 km diameter positioned within the transition zone, centred at 550 km depth. While the shallow and transition-zone structures are quite well recovered, the lower mantle structures are not as well resolved and smeared upwards.

Part 4– Seismic ratios and thermal interpretation

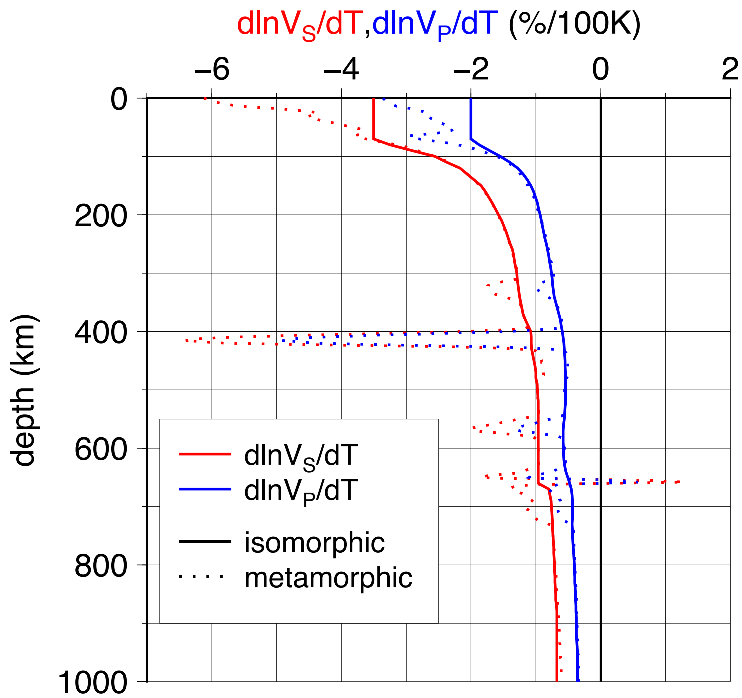

Figure S12. *P* and *S* velocity-temperature derivatives used to set up our synthetic plume resolution tests (Fig. 3) and perform our conversion of imaged velocity to temperature anomalies (Fig. 7). The dotted profiles are full (metamorphic) derivatives that include the effects of phase transitions. They were computed using PerPleX [*Connolly*, 2005] along a 1300°C adiabat for a pyrolite composition using mineral parameters from database stx08 [*Xu et al.*, 2008], with composite attenuation model Qg (above 400 km) [*Van Wijk et al.*, 2008] and Q6 (below) [*Goes et al.*, 2004]. The solid profiles correspond to $dV_{P,S}/dT$ derivatives that were smoothed to represent the isomorphic derivatives without the effects of phase boundary topography. For our scaling, we use the isomorphic derivatives because the differential travel-time tomography cannot resolve localized phase boundary anomalies [*Civiero et al.*, 2015]. Above 70 km depth, the isomorphic scaling is set to a constant value of -2% per 100 K for V_P and 4% per 100 K for V_S, more representative for a (cooler) lithospheric geotherm.

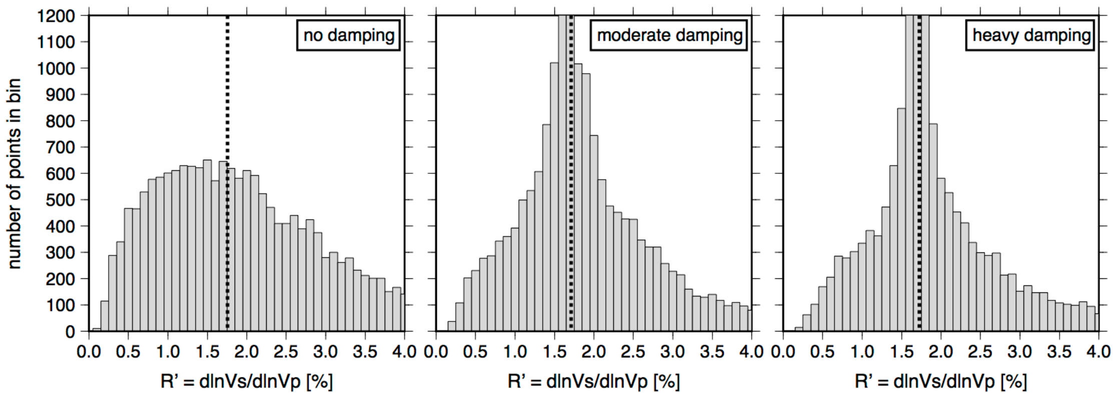

Figure S13. $R_{S,P}$ (=$\ln V_S/d\ln V_P$) distribution estimated from the NEAR-P15 *P*- and NEAR-S16 *S*-velocity models for the whole region of interest, from inversions with our preferred regularisation (flattening=4800, smoothing=153600 for both V_P and V_S) and different degrees of damping (0-35-70). For all the three differently damped models, the $R_{S,P}$ distribution is peaked around ~1.7 (median value), consistent with a dominantly thermal origin of the anomalies. As the *S* to *P* conversion used for the 3-D starting velocity model assumed the anomalies were thermal, increasing the damping parameter the $R_{S,P}$ distribution leads to a distribution more strongly peaked around this value. For each degree of damping, a large quantity of scatter around is also present and may reflect non-thermal effects and/or resolution differences between the *P* and *S* models.

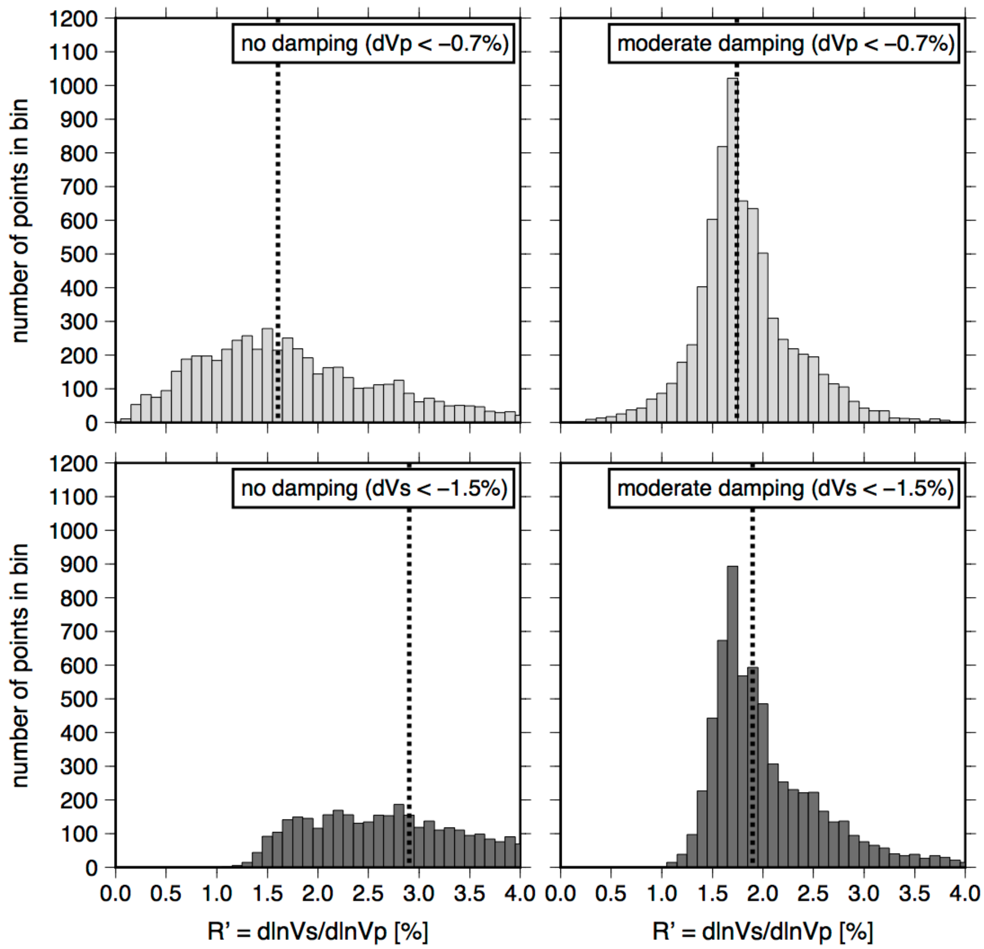

Figure S14. $R_{S,P}$ distributions calculated only for the lowest NEAR-P15 *P*- wave velocities (top panels) and NEAR-S16 *S*-wave velocities (bottom panels) (dV_P < -0.7% and dV_S < -1.5% respectively) in undamped models (first column) and moderately damped (damping=35) models (second column). $R_{S,P}$ distributions shift towards higher values compared to the distributions that include slow and fast anomalies in Fig. S13, as might be expected if the anomalies are thermal in nature, but also if some of the low velocities are due to the presence of fluids/melt.

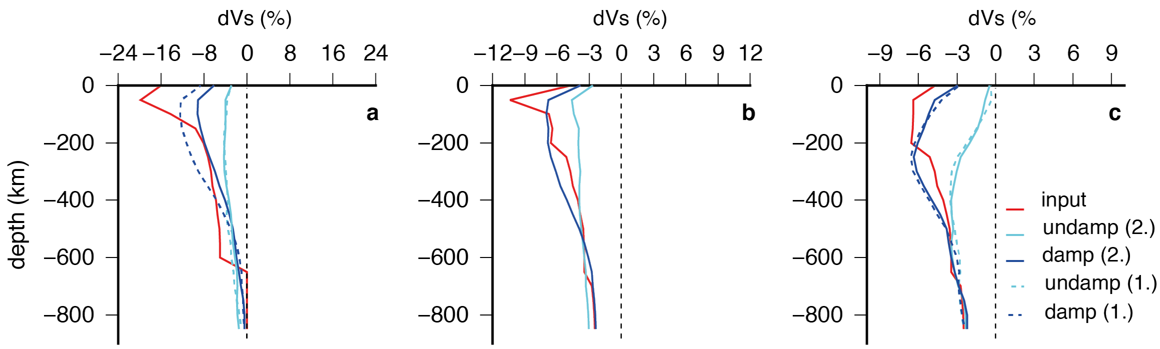

Figure S15. Profiles through the centre of the three synthetic plume models from Fig.3, a) Superplume, b) single plume, c) double plumes, showing the input and retrieved anomalies. Locations for plumes 1 (approximately MER) and 2 (Afar) for case c are shown on panel m of Fig. 3.

Part 5 – Station information

Stat	*Network*	*Lat(°)*	*Long(°)*	*Elev(km)*
AAIR	YI	-9.95	33.9	0.53
AAUS	AF,XI	9.03	38.77	2.25
ABAE	ZF,ZR	13.35	39.76	1.45
AD02	ZK	11.35	40.69	0.52
AD04	ZK	11.54	40.84	0.48
AD05	ZK	11.61	40.91	0.45
AD07	ZK	11.73	40.99	0.40
AD08	ZK	11.78	41.03	0.39
AD09	ZK	11.82	41.05	0.39
AD10	ZK	11.90	41.14	0.37
AD11	ZK	11.74	41.3	0.37
AD14	ZK	11.94	41.45	0.42
AD15	ZK	11.88	41.71	0.09
AD16	ZK	11.82	41.75	0.12
AD17	ZK	11.74	41.84	0.15
AD18	ZK	11.91	41.79	0.45
ADBA	XW	13.55	44.84	0.70
ADEE	YJ	7.79	39.91	2.48
ADEN	XW	12.78	44.98	0.06
ADHO	YR	17.24	54.28	0.91
ADTE	ZF	11.12	40.76	0.51
ADUA	XW	15.00	48.97	1.38
ADUE	YJ	8.54	38.9	1.75
ADYE	ZF	13.64	38.98	1.86
AFME	ZE,ZR	13.20	40.86	-0.06
AHME	ZR	14.09	40.28	0.05
AKEE	ZF	10.89	39.17	3.23
ALE	YR	9.42	42.03	2.03
ALGU	XW	13.05	44.93	0.1
AMBA	XW	-8.11	33.26	1.42
AMME	YJ	8.30	39.09	1.67
ANGA	XI	-2.50	36.8	0.00
ANID	XW	15.47	43.2	0.15
ANKE	YJ	9.59	39.73	2.98
ARBA	XI	6.07	37.56	1.27
ARCH	YI	-10.02	33.93	0.5
AREE	YJ	8.94	39.42	1.83
ARUT	XW	15.16	51.03	0.02
ASE	7C	11.00	42.1	0.36
ASSE	YR	13.06	42.65	0.02
ASYE	ZF,ZR	11.56	41.44	0.37
ATD	G	11.53	42.85	0.61
AWRE	YZ	12.07	40.07	0.85
AYDO	YR	16.99	53.36	0.04
AYNO	YR	17.26	53.89	0.86
BAHI	XI	11.57	37.39	1.79
BANO	YR	17.69	54.44	0.46
BARE	ZE	12.64	40.36	0.34
BARI	XI	0.47	35.98	1.01
BEDE	YJ	8.91	40.77	1.71
BELA	XI	6.93	38.47	1.92
BEND	ZP	0.58	31.39	1.35
BERE	ZE	12.17	41.19	0.57
BIHA	ZP	-2.64	31.32	1.46
BIRH	XI	9.67	39.53	2.81
BKBA	ZP	-1.36	31.81	1.27
BOBE	ZF	10.38	42.57	0.94
BOKO	XI	-2.26	37.73	0.98
BORE	YJ	8.75	39.55	1.25
BOVE	YZ	12.66	40.52	0.76
BREE	ZE	12.17	41.19	0.58
BTIE	ZF,ZR	11.19	40.02	1.66
BURO	UN	0.86	30.17	0.98
BUTE	YJ	8.12	38.38	2.09
BUTI	ZP	1.82	31.33	0.62
C01	Z5	1.36	29.76	0.95
C02	Z5	0.85	29.61	1.08
C03	Z5	0.7	29.52	1.05
C04	Z5	0.66	29.88	0.85
C05	Z5	0.48	29.5	1.20
C06	Z5	0.32	29.75	1.18
C07	Z5	0.29	29.34	1.18
C08	Z5	0.12	29.28	1.69
C09	Z5	-0.14	29.6	0.95
C10	Z5	-0.16	29.23	1.87
CAYE	YR	14.86	39.31	2.44

CHAE	YJ	9.31	38.76	2.65
CHEF	XI	6.16	38.21	1.70
CHIE	ZE	11.6	40.02	0.94
CHIM	ZP	-8.83	34.03	1.10
CLIN	YI	-9.96	33.81	0.54
DABI	XW	15.13	44.27	2.38
DAHO	YR	17.53	54.35	0.54
DALA	XW	13.73	44.74	1.44
DALE	ZR	14.23	40.22	-0.10
DAME	ZR	11.69	40.96	0.42
DAMT	XW	14.09	44.68	1.90
DAMY	GE	14.57	44.39	2.49
DEBE	YJ	8.78	39	1.91
DELE	XI	8.44	36.33	1.97
DERU	XW	16.84	51.83	0.88
DICE	ZF	11.91	41.57	0.46
DIGE	ZE	12.33	40.27	0.68
DIKE	YJ	8.06	39.56	2.75
DKUM	XW	13.27	44.76	0.4
DMRK	XI	10.31	37.73	2.36
DMTO	YR	17.73	55.07	0.44
DODT	AF	-6.19	35.75	1.11
DOLE	YR	15.1	39.98	0.09
DONE	YJ	8.51	39.55	1.31
DSS	YR	11.12	39.64	2.55
E31	XJ	8.78	39.86	1.01
E33	XJ	8.93	39.93	0.98
E34	XJ	7.21	38.6	1.93
E35	XJ	9.13	40.17	0.85
E36	XJ	9.11	40.01	0.77
E37	XJ	8.17	38.7	1.8
E39	XJ	9.24	40.13	0.77
E40	XJ	9.36	40.22	0.74
E41	XJ	8.01	38.53	1.91
E42	XJ	8.88	40.1	1.06
E43	XJ	9.25	39.5	3.29
E46	XJ	8.71	39.69	1.24
E47	XJ	8.46	39.45	1.45
E48	XJ	7.62	38.99	2.61
E50	XJ	8.27	39.5	2.07
E51	XJ	8.15	39.35	2.08

E53	XJ	8.04	39.01	1.70
E54	XJ	8.12	39.14	2.08
E55	XJ	8.3	38.95	1.68
E56	XJ	8.46	39.06	1.64
E57	XJ	8.58	39.13	1.82
E58	XJ	8.69	39.18	2.06
E59	XJ	8.71	39.35	1.68
E60	XJ	8.62	39.45	1.63
E61	XJ	8.9	39.62	1.16
E63	XJ	8.26	39.24	1.78
E65	XJ	8.4	39.21	1.55
E66	XJ	9.03	39.53	1.72
E67	XJ	8.38	39.68	2.14
E68	XJ	8.78	39.26	2.29
E69	XJ	7.93	38.72	1.68
E70	XJ	8.88	39.15	2.23
E71	XJ	8.69	38.9	1.98
E72	XJ	8.49	39.83	1.58
E73	XJ	7.74	39.03	2.5
E75	XJ	7.91	38.95	1.75
E76	XJ	7.72	38.65	1.67
E77	XJ	7.86	38.79	1.67
E78	XJ	8.59	39.7	1.22
E79	XJ	7.63	38.71	1.59
E80	XJ	8.48	39.31	1.66
E82	XJ	8.85	40.01	0.97
E83	XJ	7.8	38.79	1.90
E84	XJ	8.7	39.4	1.54
E85	XJ	8.46	39.59	1.32
EITE	YR	15.24	38.78	2.17
ELLE	ZF	11.26	40.38	0.67
ERTE	ZF,ZR	13.45	40.5	-0.01
EYUN	XW	14.78	49.27	0.18
FAME	YR	13.57	41.52	0.62
FASH	XW	15.44	50.95	0.14
FICH	XI	9.78	38.74	2.83
FINE	ZE,ZR	12.07	40.32	0.78
FOPO	ZP	0.66	30.28	1.53
FURI	IU	8.9	38.68	2.56
GALE	ZR	13.73	40.39	-0.09
GASE	ZF	11.68	38.92	2.97

GDR	YR	12.56	37.45	2.1
GEAN	XW	16.71	49.52	0.97
GEIT	ZP	-2.88	32.22	1.28
GEWE	YJ,ZF	10	40.57	0.6
GHAD	XW	16.25	52.21	0.05
GHDI	XW	15.64	52.16	0.03
GLUM	ZU	-2.62	36.19	1.30
GOBA	XI	7.03	39.98	2.73
GOMA	XD	-4.84	29.69	0.88
GTFE	YJ	9	39.84	1.04
GUDE	XI	8.97	37.77	2.02
GULE	ZR	13.69	39.59	2.02
HADO	YR	17.22	55.19	0.09
HAHY	XW	15.21	49.09	1.08
HALE	ZF,ZR	13.84	40.01	0.23
HAMA	ZP	-3.83	32.64	1.23
HATT	XW	17.32	52.11	0.77
HAYO	YR	17.18	53.34	0.83
HERO	XI	7.03	39.28	2.37
HIRN	XI	9.22	41.11	1.82
HOSA	XI	7.56	37.86	2.31
HOTA	XW	13.06	44.88	0.13
HUMY	UN	0.76	30.04	1.00
HYNE	ZF	9.31	42.1	1.98
IGRE	ZR	12.25	40.46	0.68
INEE	YJ	9.9	39.14	2.69
IRIN	ZP	-7.76	35.69	1.56
ITOJ	UN	0.84	30.23	1.00
JIMA	XI	7.68	36.83	1.66
JNJA	ZP	0.45	33.18	1.13
KABA	UN	0.78	30.13	0.92
KABE	UN	0.87	30.47	1.3
KAGO	UN	0.68	30.46	1.52
KAKA	XI	0.56	34.8	1.48
KARE	XW	17.16	51.93	0.09
KARE	YJ	10.42	39.93	0.86
KARU	UN	0.79	30.22	1.11
KAS2	UN	-0.03	30.15	0.92
KASS	UN	0.58	30.31	1.50
KBLE	ZP	-1.25	29.99	1.88
KERM	ZU	-2.83	35.98	1.14

KGMA	ZP	-4.88	29.63	0.82
KHAW	XW	13.81	43.25	0.01
KHLA	XW	13.8	44.81	1.46
KIBA	XD	-5.32	36.57	1.50
KIBE	XD	-5.38	37.48	1.00
KIBO	ZP	-3.58	30.71	1.49
KIG	AF	-1.96	30.06	1.54
KILE	UN	0.21	30.01	1.35
KINY	UN	0.51	30.13	1.70
KISA	UN	0.59	30.74	1.29
KITU	XI	-1.37	38.00	1.13
KMBO	GE	-1.13	37.25	1.94
KMTW	UN	0.74	30.38	1.56
KOBE	ZF	12.15	39.63	1.51
KOMO	XD	-3.84	36.72	1.11
KOND	XD	-4.90	35.8	1.42
KOTE	YJ	9.39	39.4	2.87
KOZE	ZR	12.49	40.98	0.54
KR42	XI	0.04	35.73	2.16
KTWE	AF	-12.81	28.21	1.23
KYLA	ZP	-9.60	33.87	0.50
LAEL	ZP	-8.57	32.06	1.60
LALE	ZF	12.03	39.04	2.42
LAVE	ZR	13.60	40.66	0.60
LBB	AF	-11.63	27.49	1.28
LEME	YJ	8.61	38.61	2.11
LODK	GE	3.42	35.36	0.67
LONG	XD	-2.73	36.7	1.38
LOSS	ZP	-8.42	33.16	1.20
LSZ	IU	-15.28	28.19	1.2
LUGH	YI	-10.03	32.83	0.59
LULE	ZR	11.99	40.7	0.59
LUSA	XW	16.49	52.57	0.05
LWND	ZF	-2.75	36.04	1.07
LYDE	ZF	12.05	41.93	0.43
MADO	YR	17.2	54.38	0.83
MAFI	ZP	-8.31	35.31	1.87
MAKA	ZP	-8.85	34.83	1.69
MALE	ZP	1.07	34.17	1.13

MAUS	ZP	-2.74	36.7	1.33
MAWI	XW	15.47	43.52	1.88
MAYE	ZF,ZR	12.78	39.53	2.44
MBAR	II	-0.6	30.74	1.39
MBWE	XD	-4.96	34.35	1.1
MDYO	YR	17.46	53.36	0.57
MECE	YJ	8.59	40.32	1.77
MEGE	ZE	11.49	41.34	0.35
MEKE	YJ	8.16	38.83	1.90
MELE	YJ	9.31	40.2	0.76
MGOR	ZP	-6.83	37.67	0.50
MIKU	ZP	-7.40	36.99	0.52
MILE	ZE	11.42	40.76	0.49
MIRA	UN	0.66	30.57	1.38
MISE	ZF	9.24	40.76	1.31
MITU	XD	-6.02	34.06	1.57
MKRE	ZP	-4.28	30.42	1.18
MLBA	ZP	-1.84	31.67	1.34
MOKA	XW	13.31	43.26	0.03
MSEY	II	-4.67	55.48	0.47
MTOR	XD	-5.25	35.4	1.10
MUGO	YR	16.90	53.77	0.04
MUKA	XW	14.49	49.04	0.04
MWEY	UN	-0.19	29.9	0.96
MZM	AF	-11.43	34.03	1.26
NAB1	YW	13.39	41.66	1.33
NAB2	YW	13.43	41.71	1.21
NAB3	YW	13.38	41.75	1.28
NAB4	YW	13.48	41.68	0.70
NAB5	YW	13.32	41.71	1.27
NAB6	YW	13.44	41.64	0.96
NAB8	YW	13.33	41.8	0.66
NAMA	ZP	-7.51	31.04	1.56
NARO	XI	-1.07	35.87	1.92
NAZA	XI	8.57	39.29	1.73
NBI	AF	-1.27	36.8	1.71
NDEI	XI	-2.69	38.17	0.73
NEKE	XI	9.09	36.52	2.08
NGIT	UN	0.64	30.03	0.99
NJOM	ZP	-9.37	34.79	1.95

NNMO	YR	17.36	54.25	0.69
NURE	YJ	8.73	39.8	1.18
NYAN	UN	0.21	30.45	1.30
PAND	XD	-8.98	33.24	1.25
PIGI	ZP	0.23	32.32	1.25
PNDA	ZP	-6.35	31.06	1.07
POLI	YI	-9.77	33.87	0.47
PUGE	XD	-4.71	33.18	1.35
QALY	YR	12.7	53.49	0.04
QATE	ZF	9.38	41.47	2.15
QISH	XW	15.51	51.69	0.06
RAHO	YR	17.06	53.81	1.18
RAND	7C	11.85	42.66	0.88
RAYN	II	23.52	45.5	0.63
RODE	ZE	12.84	40.98	0.05
ROTI	ZP	1.63	33.6	1.11
RUGA	UN	-0.26	30.1	1.36
RUNG	XD	-6.94	33.52	1.23
RWEB	UN	0.32	30.49	1.28
SAAH	XW	15.57	48.86	0.78
SAHO	YR	17.11	54.68	1.18
SAKA	ZP	-0.32	31.74	1.26
SANA	XW	15.39	44.21	2.25
SAUM	XW	16.14	49.29	0.58
SAY	YR	15.35	44.2	2.25
SAYT	XW	15.22	51.25	0.06
SCH	YI	-10.18	34.03	0.52
SEHE	ZE	12.04	40.98	0.36
SEKE	ZF	12.62	39.03	2.26
SELA	XI	7.97	39.13	2.30
SEMP	UN	0.84	30.17	1.30
SENE	YJ	9.15	39.02	2.56
SEYU	XW	15.93	48.8	0.68
SHEE	YJ	10.00	39.89	1.30
SHIB	XW	15.5	43.91	2.63
SHIO	YR	17.19	54.17	0.55
SHUH	XW	15.61	50.92	0.26
SILE	II,ZE	12.41	41.19	0.48
SIMA	XW	17.56	52.32	0.66
SING	XD	-4.64	34.73	1.46

SMRE	ZF	13.20	39.21	1.98
SONG	ZP	-10.67	35.65	1.12
SOOO	YR	17.08	54.88	0.14
SRDE	ZF	11.96	41.31	0.09
SUGH	XW	14.80	43.44	0.25
SULU	ZP	-4.57	30.09	0.09
SUMB	ZP	-7.95	31.62	1.84
TABU	XW	15.93	52.14	0.02
TALE	XI	0.98	34.98	1.82
TAMU	XW	17.29	49.93	0.67
TARA	XD	-3.89	36.02	1.27
TARI	XW	16.05	48.98	0.62
TAWI	XW	15.48	43.72	2.33
TEBE	AF	0.05	32.48	1.13
TEND	XI	11.79	41.00	0.42
TERC	XI	7.14	37.17	1.39
TEZI	AF	-15.75	26.02	1.12
TINA	XW	16.53	52.08	0.20
TIOE	YR	14.67	40.87	0.04
TQHO	YR	17.06	54.43	0.04
TRUE	ZE,ZR	12.48	40.31	0.38
TUND	ZP	-9.30	32.77	1.66
U01	Z5	0.99	30.32	0.69
U02	Z5	-0.31	29.86	0.92
U03	Z5	-0.6	29.82	1.09
U04	Z5	0.34	30.04	1.64
U05	Z5	0.38	30.22	1.12
U06	Z5	0.19	30.45	1.27
U07	Z5	0.49	30.33	1.42
U08	Z5	-0.14	29.87	0.95
U09	Z5	0.02	30.08	0.91
U10	Z5	-0.1	30.38	1.41
U11	Z5	-0.44	30.56	1.45
U12	Z5	-0.53	30.16	1.65
U13	Z5	0.64	30.65	1.37
U14	Z5	0.71	30.06	0.95
U15	Z5	0.81	30.14	0.71
U16	Z5	0.69	30.28	1.56
U17	Z5	0.56	30.17	1.61
U18	Z5	0.73	30.37	1.56
U19	Z5	0.91	30.36	0.73
U20	Z5	0.03	29.77	1.24
U21	Z5	-0.28	30.04	1.00
U22	Z5	0.21	30.01	1.34
U23	Z5	0.35	29.89	4.45
UAYA	XW	15.71	42.69	0.01
URAM	XD	-5.09	32.08	1.12
UVZA	ZP	-5.10	30.39	0.99
WANE	XI	10.17	40.65	0.61
WASH	XI	8.99	40.17	0.83
WASH	XW	16.34	49.51	0.83
WELK	XI	8.29	37.78	1.90
WINO	ZP,ZE	-9.76	35.30	1.51
WLDE	ZF	11.82	39.59	1.88
WOLE	YJ	8.53	37.98	2.06
WUCE	ZF	11.51	39.61	1.91
YAF	YR	13.87	45.25	2.27
YAYE	ZF	11.86	38.00	2.63
YSLE	XW	14.94	44.28	2.56
ZOMB	AF	-15.38	35.35	0.89
ZUWA	XW	15.73	43.02	0.09

Table S1. All seismic stations (station code, network code, latitude, longitude and elevation) used in the *S-SKS* tomographic inversion

References

Civiero, C., J. O. S. Hammond, S. Goes, S. Fishwick, A. Ahmed, A. Ayele, C. Doubre, B. Goitom, D. Keir, and J. Kendall (2015), Multiple mantle upwellings in the transition zone beneath the northern East-African Rift system from relative P-wave travel-time tomography, *Geochem. Geophys. Geosyst., 16*(9), 2949-2968.

Connolly, J. A. D. (2005), Computation of phase equilibria by linear programming: A tool for geodynamic modeling and its application to subduction zone decarbonation, *Earth Planet. Sci. Lett., 236*(1–2), 524-541.

Fishwick, S. (2010), Surface wave tomography: Imaging of the lithosphere–asthenosphere boundary beneath central and southern Africa?, *Lithos, 120*(1–2), 63-73.

Goes, S., F. Cammarano, and U. Hansen (2004), Synthetic seismic signature of thermal mantle plumes, *Earth Planet. Sci. Lett., 218*(3–4), 403-419.

Hammond, J. O. S., et al. (2013), Mantle upwelling and initiation of rift segmentation beneath the Afar Depression, *Geology, 41*(6), 635-638.

Van Wijk, J., J. Van Hunen, and S. Goes (2008), Small-scale convection during continental rifting: Evidence from the Rio Grande rift, *Geology, 36*(7), 575-578.

Xu, W., C. Lithgow-Bertelloni, L. Stixrude, and J. Ritsema (2008), The effect of bulk composition and temperature on mantle seismic structure, *Earth Planet. Sci. Lett., 275*(1-2), 70-79.